

Structural, dielectric, and electrical transport properties of Al³⁺ substituted nanocrystalline Ni-Cu spinel ferrites prepared through the sol-gel route

M. M. Rahman^a, N. Hasan^b, M. A. Hoque^c, M. B. Hossen^d, M. Arifuzzaman^{e,*}

^aDepartment of Industrial and Production Engineering, Bangladesh University of Textiles, Dhaka-1208, Bangladesh

^bDepartment of Electrical and Computer Engineering, North South University, Dhaka-1229, Bangladesh

^cBangladesh Council of Scientific and Industrial Research, Dhaka-1205, Bangladesh

^dDepartment of Physics, Chittagong University of Engineering and Technology, Chattogram-4349, Bangladesh

^eDepartment of Mathematics and Physics, North South University, Dhaka-1229, Bangladesh

*Corresponding author:

M. Arifuzzaman (md.arifuzaman01@northsouth.edu)

Abstract

In this study, a series of nanocrystalline ferrites of $\text{Ni}_{0.7}\text{Cu}_{0.30}\text{Al}_x\text{Fe}_{2-x}\text{O}_4$ ($x=0.00$ to 0.10 with a step of 0.02) has been synthesized through the sol-gel auto combustion technique. The structural, morphological, dielectric, and electrical properties of the Ni-Cu spinel ferrite nanoparticles are analyzed due to the substitution of Al^{3+} content. The crystalline and structural characteristics of the prepared nanoparticles (NPs) have been studied employing the x-ray diffraction (XRD) spectra and FTIR analysis. The extracted XRD patterns assure the single-phase cubic spinel structure of all samples with homogeneity and no impurity, which indicates the yielding of high crystalline NPs. The average crystallite size of the synthesized ferrite nanoparticles is found in the range ($55.63\text{--}70.74$ nm) and the average grain size varies from 59.00 to 65.00 nm. FTIR study also confirms the formation of spinel structures in the prepared Ni-Cu ferrite nanoparticles. A slight decrease of average grain size with increment of Al^{3+} content is observed in the surface morphological study carried out by the field emission scanning electron microscopy (FESEM). The studied materials are found in semi-spherical shapes, showing the multi-domain grains separated by grain boundaries with some agglomerations. The chemical composition study for the synthesized Ni-Cu spinel ferrites using energy dispersive x-ray (EDX) ensures the presence of each component in appropriate proportions in each sample. The dielectric dispersion nature of all investigated materials is reflected in the current study up to the frequency of 10 kHz. Because of the high resistive grains, the value of ϵ' is higher at low frequencies, resulting in space charge polarization. However, the effect of cation distributions on A and B sites on the grain dependent space charge polarization nature is reflected in the dielectric constant. The sample with $x = 0.1$ demonstrates that the space charge polarization has increased, resulting in a higher dielectric constant value. The impedance spectroscopy confirms the non-Debye relaxation phenomena of the synthesized nanomaterials. The contribution of grains and grain boundaries is resolved through the modulus study of the materials, which reconfirms their dielectric relaxation. The trend in variation of AC resistivity suggests the normal behavior of the materials with varying frequencies, which is

explained by the hopping mechanism.

Keywords: Spinel nano-ferrites; Sol-gel process; XRD; FTIR; FESEM; Impedance spectroscopy; Dielectric dispersion; AC resistivity.

1. Introduction:

Magnetic ferrite nanoparticles in the spinel phase have been considered as the influential class of materials, which are employed in various high-frequency device applications¹. The cubic spinel structure has the chemical formula of AB_2X_4 , where the anions X are occupied by O atom as of metal oxides forming the cubic close-packed lattice, tetrahedral interstices fill the A site as the ‘network formers’ and octahedral interstices occupy the B site as the ‘modifiers’, called the Ferro-spinel and semiconductor in nature²⁻⁵. Most spinel ferrites belong to the space group of $Fd3m$ (No. 227, $Z = 8$), which provide the highest symmetrical face-centered cubic (FCC) spinel structure. A spinel unit supercell's crystal is formed by 8 A-sites and 16 B-sites cations. Based on the distribution of divalent metal ions and trivalent ferric ions over A and B sites, spinel ferrites are of three classes; normal spinel, inverse spinel, and mixed spinel⁶.

Magnetically soft spinel ferrites are used in a large spectrum of biomedical and industrial applications including medical treatments, such as magnetic resonance imaging, antenna fabrication, computer memories, energy storage in supercapacitors, high-density information storage, high-frequency transformers, hyperthermia treatment, multi-layered chip inductors, water purification methods, sensing of nucleic acid, separation of DNA and RNA, gene therapy and delivery, ferrofluids and so on⁷⁻¹³. The advancement of electronic devices is now moved to integrated circuits-based technology, where highly efficient transistors are increasing gradually in accordance with Moore's law which requires nano-level engineering and fabrication. Thus, in contrast to bulk materials, researchers are now focusing on nanocrystalline ferrites' for utilizing them in the advancement of nano-technological devices. The physical and chemical characteristics of ferrite nanomaterials mostly depend on their scale size, shape, or morphology. The structural

parameters such as crystal size and lattice parameters are somehow linked to the electrical and magnetic properties of ferrite nanoparticles. Therefore, the controlling of several factors such as the particle size, surface-to-volume ratio, magnetic anisotropy eventually improves the electronic properties of magnetic nanoparticles in the spinel phase, owing to their transitions from bulk to nano-shape.

Researchers are continuously paying their efforts to employ an easy and efficient method for yielding the nanocrystalline ferrites to tailor their structural, dielectric, electric, and magnetic properties under favorable environmental conditions. Various techniques have been deployed to synthesize nanostructured ferrite materials till now viz. sol-gel auto combustion, co-precipitation, high-energy milling, hydrothermal synthesis, precursor method, mechanochemical route, and microwave hydrothermal^{7-9,14-17}. Among these, the sol-gel route appears to be a prominent method for preparing ferrite nanoparticles, as it is eco-friendly, less expensive, and effective without the involvement of expensive equipment to maintain a good stoichiometry during the synthesis process. The sol-gel is a wet chemical method, which is widely used due to its potential advantages such as enhanced control over homogeneity, elemental composition, and powder morphology with a uniform narrow particle size distribution at relatively low temperature^{7,16-18}.

Researchers attempted sporadically to study the structural, electrical, morphological, photocatalytic, and magnetodielectric properties of Ni-Cu series ferrite NPs demonstrating various effects of doping on the properties of the materials crystal. Doping is an effective method to ameliorate the applications to a broad range by achieving excellent optoelectronic properties. Investigations are still continued with selecting different atoms as dopants or substitutions in A and B- sites to tailor the physical, structural and electromagnetic properties of Ni-based mixed spinel ferrite nanoparticles¹⁹⁻²⁸. *Munir et al.*²⁹ conducted an experiment with a noble nanocomposite $\text{CuFe}_2\text{O}_4/\text{Bi}_2\text{O}_3$ by introducing Bi_2O_3 nano-petals into the porous CuFe_2O_4 and observed a significant increase in the photocatalytic activity in effect of photo-degradation activity. However, the investigated nanocomposite has remarked with an excellent magnetic separation at

room temperature for the reduced recombination and improved separation of electron-hole pairs. Carbon coated highly active magnetically recyclable hollow nano-catalysts have been synthesized by *Shokouhimehr et al.*³⁰, where the authors projected that the prepared nanocomposite can be used as a general platform for loading other noble metal catalyst nanoparticles, resulting in high yields (up to 99 percent) in selective nitroarenes reduction and Suzuki cross-coupling reactions. Furthermore, magnetic properties revealed that the catalysts could be easily separated using a suitable magnetic field and recycled five times in a row. Moreover, *Rahman et al.*³¹ thoroughly investigated the photocatalytic efficiency and recycling stability of rGO supported cerium substituted nickel ferrite nanoparticles under visible light illumination. According to their findings, NiCe_yFe_{2-y}O₄/rGO (NCFOG) nanocomposite outperformed NiCe_yFe_{2-y}O₄ nanoparticles by two times in photocatalytic efficiency and recycling stability, which is attributed to the formation of NCFOG heterojunction that enables in the separation of photo-induced charge carriers while maintaining a strong redox ability. Recently, *M. Arifuzzaman et al.*¹⁷ studied Cu substituted Ni-Cd ferrite NPs and reported the decrease of average crystallite size and saturation magnetization of Ni_{0.7-x}Cu_xCd_{0.3}Fe₂O₄ up to x=0.2. Besides, *V. A. Bharati et al.*³² reported the influence of parallel doping of Al³⁺ and Cr³⁺ on the structural, morphological, magnetic, and Mössbauer properties of Ni ferrite NPs and justified their suitability in HF device applications. In³³, *K. Bashir et al.* revealed the electrical and dielectric properties of Ni-Cu ferrite NPs with the doping of Cr³⁺, making them the potential for HF applications and photocatalytic activity. *Le-Zhong Li et al.*³⁴ examined the Al³⁺ substituted Ni-Zn-Co ferrites and observed a decrease in saturation magnetization at >0.10. They reported about the metal-semiconductor transition behavior of Ni-Zn-Co ferrites as an effect of varying temperature and the increase of dc resistivity with Al content was found. The structural and magneto-optical properties of Ni ferrite NPs were propounded in³⁵, where the authors calculated the electronic bandgap of 1.5 eV and observed a decrease in saturation magnetization and T_c with Al³⁺ content. In addition, density functional theory (DFT) based simulation was employed in estimating the electronic structure of CuO NPs with the optimized

geometric crystal calculation, which showed the variation of energy band gap with Al content in the samples ³⁶. The effect of doping materials on the characteristics of the different spinel ferrite nanoparticles are also available in the literature, Zn ferrite ^{37,38}, Ga ferrite ³⁹, Co ferrite ⁴⁰⁻⁴², Fe ferrite ⁴³, Mg ferrite ^{25,44}, and Ni-Zn ferrite ^{45,46}.

However, as per literature survey, no study has been found yet on the structural, dielectric, and electrical properties of Al^{3+} substituted nanocrystalline Ni-Cu spinel ferrites. Therefore, it is important to perceive the role of Al substitution on nano-crystallinity and the physical characteristics of Ni-Cu ferrite NPs. Henceforth, the present study aims to explore the influence of Al^{3+} substitution on the structural, dielectric dispersion and electrical conductivity properties of the synthesized nanocrystalline $\text{Ni}_{0.70}\text{Cu}_{0.30}\text{Al}_x\text{Fe}_{2-x}\text{O}_4$ ($x=0.00$ to 0.10 with a step of 0.02) ferrites through the sol-gel process.

2. Experimental details

Materials:

To synthesize the studied nanocrystalline Ni-Cu spinel ferrites, analytical-grade reagents-nickel (II) nitrate $\text{Ni}(\text{NO}_3)_2 \cdot 6\text{H}_2\text{O}$ (98%), copper (II) nitrate $\text{Cu}(\text{NO}_3)_2 \cdot 3\text{H}_2\text{O}$ (95-103%), ferric (III) nitrate $\text{Fe}(\text{NO}_3)_3 \cdot 9\text{H}_2\text{O}$ (98%), and aluminum (III) nitrate $\text{Al}(\text{NO}_3)_3 \cdot 9\text{H}_2\text{O}$ (98%) were used in this experiment which purchased from the Research-Lab Fine Chem.

2.1 Synthesis of Ni-Cu-Al nanoparticles:

Derivatives of $\text{Ni}_{0.70}\text{Cu}_{0.30}\text{Al}_x\text{Fe}_{2-x}\text{O}_4$ ($0 \leq x \leq 0.1$) nanoparticles with a step of 0.02 , were synthesized by the sol-gel process. In this process, metal materials of $\text{Ni}(\text{NO}_3)_2 \cdot 6\text{H}_2\text{O}$, $\text{Cu}(\text{NO}_3)_2 \cdot 3\text{H}_2\text{O}$, $\text{Fe}(\text{NO}_3)_3 \cdot 9\text{H}_2\text{O}$, and $\text{Al}(\text{NO}_3)_3 \cdot 9\text{H}_2\text{O}$ were taken as raw materials and dissolved them in ethanol and mixed in certain proportions with a magnetic stirrer to make a homogeneous solution. The pH of the mixture was kept at 7 using the liquid NH_4OH solution and the sol was continued to heat up to a temperature of 70°C until turning it into a form of dry gel. In an electric

oven, the dried gel was heated at 200°C for 5 hours, during which a self-ignition process occurred and the compositions gradually became fluffy-loose powder. To obtain the resulting ingredients in a highly crystalline form, the derived powder was annealed at 700°C for another 5 hours to eliminate any impurity present in the samples. The powder was further homogenized by grinding it in a hand-milling process in a mortar. A hydraulic press of 65 MPa was then applied to the samples for 2 minutes to condense and turned them into disk-shaped samples. The prepared samples were 12 mm in diameter and 2.3 mm in thickness. Powder samples were finally sent for further study on dielectric and electrical measurements.

2.2 Characterization and property measurements

The structural parameters of the yielded nanocrystalline ferrites were determined through the powder x-ray diffractometer (XRD) analysis using the model PW3040, with $\text{CuK}\alpha$ radiation of $\lambda = 1.5418\text{\AA}$. The lattice parameter, crystal size (D), and the displacement density were retrieved by using the XRD data. The theoretical density (ρ_{th}), micro-strain (ϵ_{ms}), lattice strain (ϵ_{ls}), and stacking faults in the crystal structure were also determined. The lattice parameter (a) and crystallite size (D) were measured by the following relations [20]:

$$a = d_{hkl} \sqrt{(h^2 + k^2 + l^2)} \quad (1)$$

$$D = \frac{0.9\lambda}{\beta_{hk} \cos\theta} \quad (2)$$

where, λ , β_{hkl} , θ , and d_{hkl} , respectively, indicate the wavelength of the X-ray, the full width at half maximum (FWHM) at the most prominent peak (311), the Bragg's angle, and the distance between adjacent planes. Fourier transform infrared (FTIR) spectroscopy was performed to investigate the about spinel phase in structure in all of the prepared samples. The morphology of the studied materials has been interrogated by the Field Emission Scanning Electron Microscopy (FESEM) (JEOL-JSM 7600F model). The Wynne Kerr Impedance Analyzer (model:6500B) was used to determine the complex dielectric (ϵ^*), AC resistivity (ρ_{AC}), complex electric modulus (M^*), and complex impedance (Z^*) of nanocrystalline ferrite samples.

3. Result and Discussion:

3.1 Structural analysis:

XRD patterns of Al^{3+} substituted Ni-Cu ferrites annealed at 700°C , are illustrated in Fig. 1, where the peaks are resulted due to diffractions from the planes of (111), (220), (311), (222), (400), (422), (511), and (440). The peaks are shaped well-defined with a homogeneous distribution of nanoparticles, which attest to their highly crystalline nature with no impurity. Such peaks indicate the cubic single-phase formations of the spinel materials^{32–34}. The peak diffracted from the plane (311) is found as the high intensity, which was used to determine the average crystallite size of the materials (see Table 1) using Debye-Scherrer's equation. The lattice constant (a_0) values are calculated by the Nelson-Riley technique and unit cell volumes (V) of the compositions are listed in Table 1. The decreasing trend of lattice constant and cell volume with increasing Al^{3+} content is observed, which is due to the replacement of larger ionic (0.67 \AA) cations by that with smaller radius (0.51 \AA). As Al^{3+} is replacing to the place of Fe^{3+} in the investigated ferrites, the unit cell becomes shrinkage, as a result, both a_0 and V decrease linearly with Al^{3+} content, well satisfied by Vegard's law^{47,48}. As appeared in Table 1, the average crystallite size decreases with Al^{3+} content, which might be because of the ionic radius difference between Al^{3+} and Fe^{3+} ions, offering redistribution of cations in A and B sites which ultimately cause the increase in stress and strain of the samples. Lattice spacing is determined by the following equation:

$$d = \frac{n\lambda}{2\sin\theta} \quad (3)$$

where d is the inter-spacing distance between crystal planes and the value of n is taken as 1, which represents the order of diffraction.

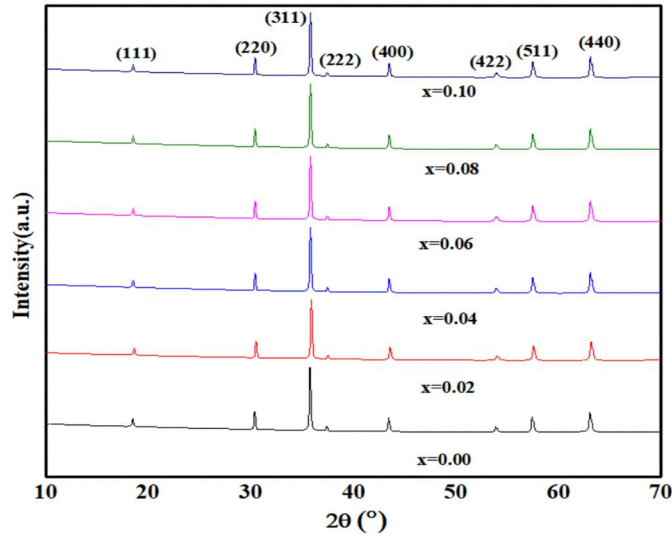


Fig. 1. XRD spectra for the synthesized $Ni_{0.7}Cu_{0.3}Al_xFe_{2-x}O_4$ ferrite nanoparticles annealed at $700^\circ C$

The sharp diffraction peaks from XRD confirms the higher crystallinity of the ferrites. The percentage of crystallinity for the prepared nanoparticles is measured by the following equation^{49,50}:

$$\% \text{ Crystallinity} = \frac{\text{Area under the crystalline peaks}}{\text{Area of the all peaks}} \times 100 \quad (4)$$

The theoretical density (ρ_{th}) is calculated by the following relation⁵¹:

$$\rho_{th} = \frac{8M_w}{N_a a_0^3} \quad (5)$$

where M_w and N_a indicate the molecular weight of the compositions and Avogadro's number, respectively. The experimental density (ρ_{ex}) is calculated by the following equation:

$$\rho_{ex} = \frac{M}{\pi r^2 l} \quad (6)$$

where M , r , and l represent the mass, radius, and height of the synthesized samples in tabloid shapes, respectively.

The experimental density and the theoretical density of the samples annealed at $700^\circ C$ are listed in Table 1. The porosity is found to increases as presented in Table 1, which is due to the discontinuity of the grain size, resulting in the decrease of density. The P (%) is calculated by the following relation:

$$P (\%) = \frac{\rho_{th} - \rho_{ex}}{\rho_{th}} \times 100 \% \quad (7)$$

The porosity is nothing but a relation between inter-granular and intra-granular porosity, which is shown by the following equation:

$$P (\%) = P_{inter} + P_{intra} \quad (8)$$

The total displacement length per unit volume of the crystal structure can be referred to as the dislocation density (δ) and the way to reduce it is to anneal the samples at high temperatures, which in turn increases their grain size [36]. This annealing is also considered as the regulator of the strength and flexibility of the crystal structure. The visible parallel lines and random lines in the crystal may indicate the displacements, which means these lines may result due to the displacement. Displacement density and particle size follow an inverse relationship with giving an error called linearity error. The dislocation density is calculated by the following equation:

$$\delta = \frac{1}{D^2} \quad (9)$$

The length due to the deformation of an object is closely related to the pressure applied, known as the lattice strain (ϵ_{ls}). The defects caused by imperfections in the crystal structure compel atoms to deviate slightly from their normal position ⁵². These structural flaws include interstitial and/or impurity atoms that cause lattice strain, which can be determined by the following relation:

$$\epsilon_{ls} = \frac{\beta}{4 \tan \theta} \quad (10)$$

where θ represents the angle of diffraction and β indicates the full width at half maximum. The stacking faults are induced in the atomic planes of the crystal because of the interruption of the layered arrangement in a normal lattice structure. The stacking fault [SF] is determined by the following equation:

$$SF = \frac{2\pi^2}{45\sqrt{3}\tan\theta} \quad (11)$$

Various defects in the crystal structure such as displacement, plastic deformation, point defects, and domain boundary defects are considered to be the key factors of the deformation in the structure and it is assumed that this deformation occurs in one part out of nearly one million parts

of the material defined as the micro strain (ϵ_{ms}). A notable feature of the micro strain is that it maximizes the peak and the following equations are introduced to comprehend it ⁵³:

$$\epsilon_{ms} = \frac{\beta \cos \theta}{4} \quad (12)$$

The ionic radii of A and B sublattices are calculated by the following relations ^{9,54}:

$$r_A = \sqrt{3}a_0(u - 0.25) - r_o \quad (13)$$

$$r_B = a_0(0.625 - u) - r_o \quad (14)$$

where r_o and u represent the radius of oxygen (1.32 Å) and oxygen parameter with the value of $\frac{3}{8}$, respectively. The distance between the centers of adjacent ions is defined as the hopping length and the lengths for A-A sites, B-B sites, and A-B sites are calculated using the following equations, respectively ^{54,55}:

$$L_{A-A} = \frac{a_o\sqrt{3}}{4} \quad (15)$$

$$L_{A-B} = \frac{a_o\sqrt{11}}{8} \quad (16)$$

$$L_{B-B} = \frac{a_o}{2\sqrt{2}} \quad (17)$$

where a_0 represents the lattice constant.

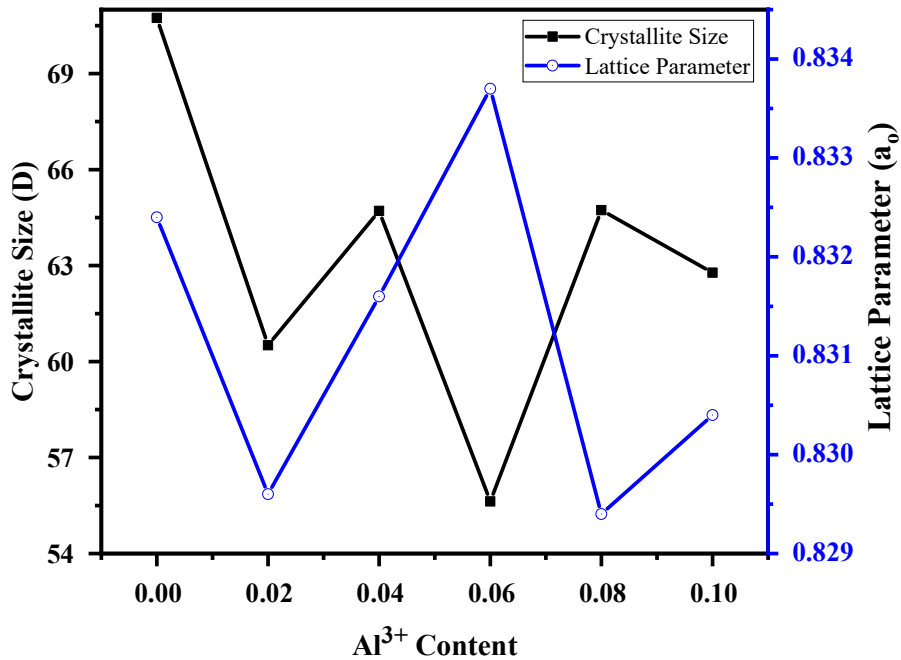


Fig. 2. Variation in lattice constant and crystallite size with Al³⁺ content.

To confirm the structure of the spinel phase in all of the prepared samples, Fourier transform infrared (FTIR) spectroscopy was utilized in this study. Fig. 3 depicts the FTIR spectra of nanocrystalline $\text{Ni}_{0.70}\text{Cu}_{0.30}\text{Al}_x\text{Fe}_{2-x}\text{O}_4$ ferrites taken in the frequency region of $450\text{-}4000\text{ cm}^{-1}$. The ν_1 and ν_2 are two fundamental strong absorption bands can be observed in effect of the metal-oxygen (M-O) bonds at the tetrahedral and octahedral sites. The entity of high frequency ν_1 band found in the range of $585\text{-}615\text{ cm}^{-1}$ which is formed by the internal stretching vibration of the M-O bonds at tetrahedral sites whereas the low frequency ν_2 band around 400 cm^{-1} corresponds to that of octahedral site ⁵⁶. The formation of spinel structures in the prepared Ni-Cu ferrite nanoparticles is ascertained by the observed bands. The bands observed in this investigation is consistent with previous findings. ^{57,58}. The absorption peaks, however, are induced by the tetrahedral site of the metal's intrinsic stretching vibration. Moreover, the stretching vibration of M-O at both sites is influenced by changes in the lattice parameter. The tetrahedral stretching frequency band (ν_1) shifts to higher frequency regions as Al^{3+} doping increases, as observed from the FTIR spectra. As illustrated from the Fig. 3, the observed band shifting with changing of Al^{3+} concentrations might be due cations distribution followed by lighter Al^{3+} substitution over the tetrahedral and octahedral sites ^{56,58,59}.

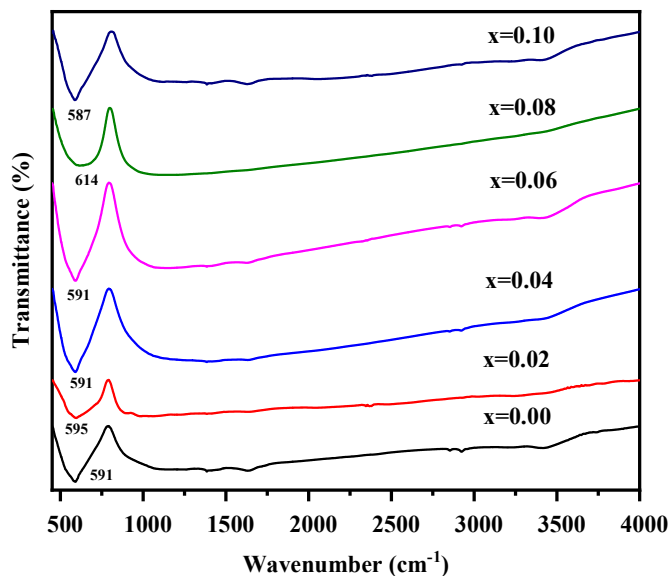


Fig 3. Room temperature FTIR spectra of the synthesized Ni-Cu spinel ferrite nanoparticle with Al^{3+} concentrations

3.2 FESEM and EDX Studies

Fig. 4 shows the FESEM micrographs of nanocrystalline $Ni_{0.70}Cu_{0.30}Al_xFe_{2-x}O_4$ annealed at 700 °C. As depicted in all figures of Fig. 4 (A-F), the grains are found in semi-spherical shapes with a uniform and even distribution in multi-domains separated by grain boundaries. The average grain size of the synthesized ferrite nanoparticles is measured by ⁵⁴:

$$G_a = \frac{1.5L}{XN} \quad (18)$$

where L, X, respectively, indicate the total length in cm and the magnification of the micrographs, and N is the number of intercepts. Fig. 5 illustrates the EDX analysis of $Ni_{0.70}Cu_{0.30}Al_xFe_{2-x}O_4$, which ensures the presence of each and every component in each sample with appropriate proportions. The expected sum of each of the observed compositions is found 100%, which confirms the accuracy of the sol-gel analysis technique and manifests its novelty.

Table 1. Structural parameters of nanocrystalline $Ni_{0.7}Cu_{0.3}Al_xFe_{2-x}O_4$ varying Al^{3+} content.

Parameters	x = 0.00	x = 0.02	x = 0.04	x = 0.06	x = 0.08	x=0.10
d (nm)	0.2510	0.2502	0.2508	0.2514	0.2501	0.2504
a ₀ (nm)	0.8324	0.8296	0.8316	0.8337	0.8294	0.8304
D (nm)	70.74	60.51	64.71	55.63	64.73	62.78
V (nm ³)	0.5768	0.5711	0.5752	0.5795	0.5705	0.5727
% Crystallinity	87.10	93.83	94.92	97.29	94.10	94.38
δ ($\times 10^{14}$) (lines/m ²)	1.998	2.731	2.338	3.230	2.387	2.538
ϵ_{LS} ($\times 10^{-3}$)	1.597	1.860	1.744	2.033	1.738	1.795
SF	0.446	0.445	0.446	0.446	0.445	0.445
ϵ_{ms} ($\times 10^{-4}$) (line ⁻² /m ⁻⁴)	4.9	5.729	5.357	6.230	5.355	5.220
ρ_{ex} (kg/m ³) ($\times 10^3$)	3.832	3.832	3.832	3.832	3.832	3.832
ρ_{th} (kg/m ³) ($\times 10^3$)	5.256	5.297	5.247	5.195	5.264	5.230
P (%)	27.093	27.657	26.968	26.237	27.204	26.730
G _a (nm)	59	64	65	62	61	62
r _A (nm)	0.0482	0.0476	0.0481	0.0485	0.0476	0.0478
r _B (nm)	0.0761	0.754	0.0759	0.0764	0.0753	0.0756
L _{A-A} (nm)	0.3605	0.3605	0.3605	0.3605	0.3605	0.3605
L _{A-B} (nm)	0.3451	0.3451	0.3451	0.3451	0.3451	0.3451
L _{B-B} (nm)	0.2943	0.2943	0.2943	0.2943	0.2943	0.2943

3.3 Dielectric Property

Fig.6 (A, B) demonstrates the variation in real (ϵ') and imaginary (ϵ'') parts of complex dielectric constant of nanocrystalline $Ni_{0.70}Cu_{0.30}Al_xFe_{2-x}O_4$ annealed at 700 °C with increasing frequency. The dielectric property of ferrites is contingent on different factors such as preparation method, chemical composition, grain size, electronic di-polarity, and so on. The ϵ' , ϵ'' , and dielectric loss tangent ($\tan \delta_E$) are calculated by the following relations:

$$\varepsilon' = \frac{Ct}{\varepsilon_o A} \quad (19), \quad \varepsilon'' = \varepsilon' \tan \delta_E \quad (20), \text{ and } \tan \delta_E = \frac{1}{\omega \varepsilon_o \varepsilon' \rho} \quad (21)$$

where C is the capacitance, $\omega = 2\pi f$, f represents the applied field frequency, ε_o represents the free-space permittivity, t is the thickness and A is the area of the contact surface of the tabloids.

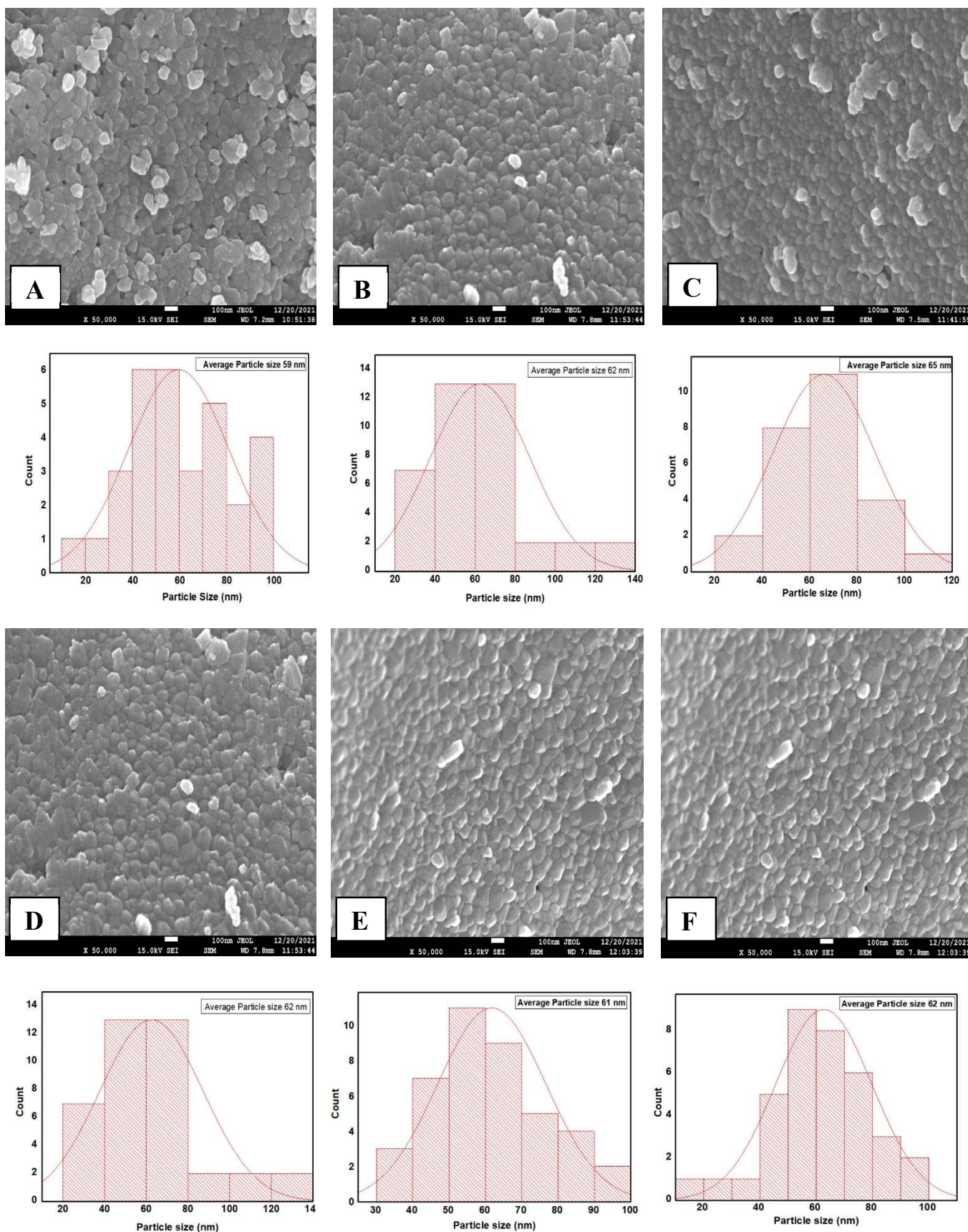


Fig. 4. FESEM micro-graphs and corresponding histogram analysis of the synthesized $Ni_{0.7}Cu_{0.3}Al_xFe_{2-x}O_4$ NPs; ((A) $x=0.00$, (B) $x=0.02$, (C) $x=0.04$, (D) $x=0.06$, (E) $x=0.08$, and (F) $x=0.10$)).

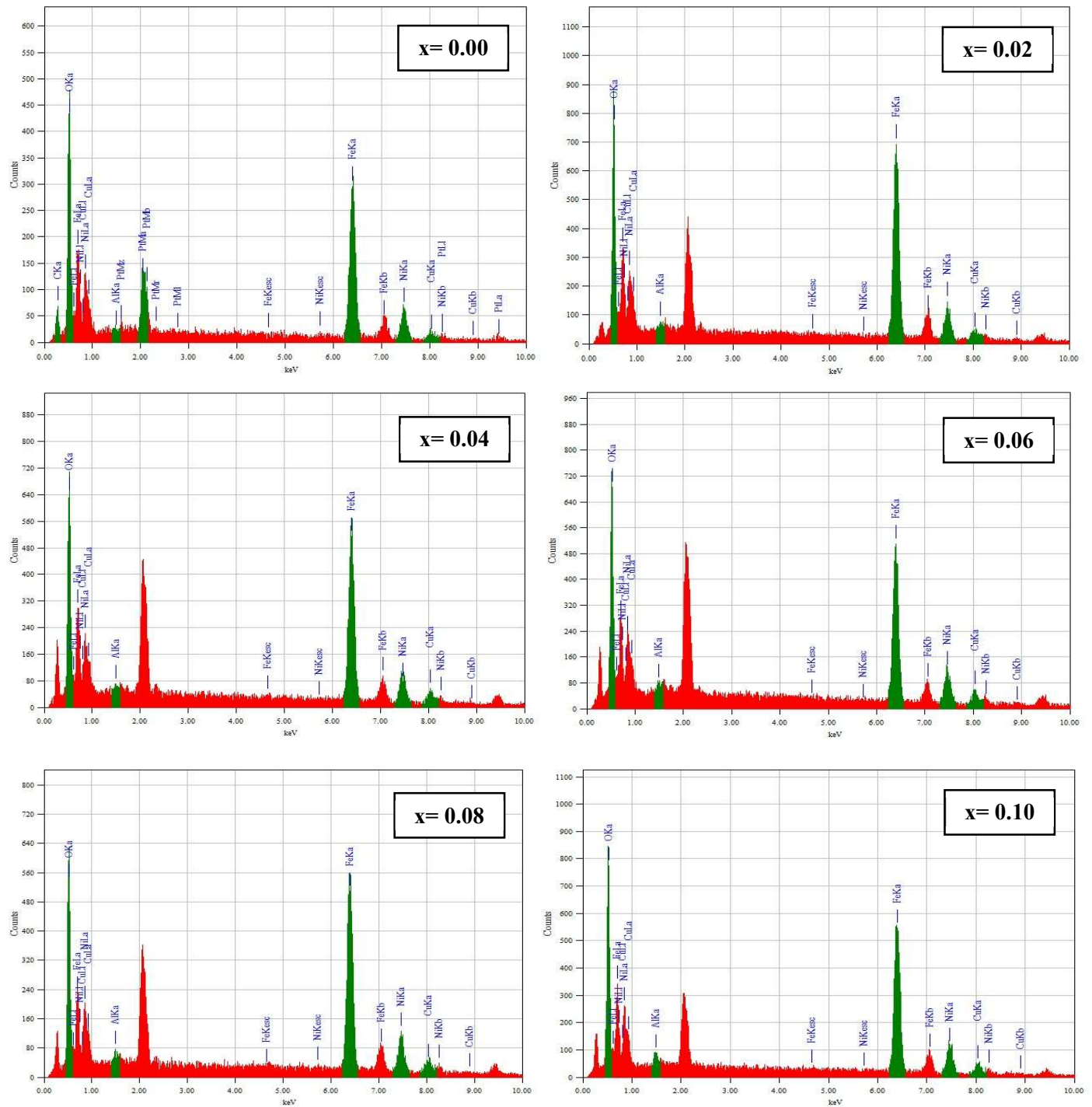


Fig. 5. Energy dispersive spectra (EDX) of the prepared Al^{3+} substituted nanocrystalline $\text{Ni}_{0.7}\text{Cu}_{0.3}\text{Al}_x\text{Fe}_{2-x}\text{O}_4$.

Fig. 6(A) illustrates that ϵ' decreases with the frequency up to 10^5 Hz and thereafter remains almost constant with showing a very low value. On the contrary, the imaginary part (ϵ'') reveals higher values at low frequency regime and decreases vigorously with frequency as observed in Fig. 6(B). The observed dispersive dielectric nature of these investigated materials can be described by the

Maxwell–Wagner interfacial theory of polarization supported with the Koop’s phenomenological theory^{54,55,60}. The grain boundaries are more active at low frequencies, whereas at high frequencies grains are more contributing. At the low frequency, the value of ϵ' is higher because of the high resistive grains, which gives the space charge polarization^{47,48}. The decrease of real dielectric constant (ϵ') with increasing frequency is found in Fig. 6A, because the grains come into action at higher frequencies and the hopping electrons cannot follow the applied electric field, causing the polarization to decrease, and the value of ϵ' appears to be very low, becoming almost constant⁶¹.

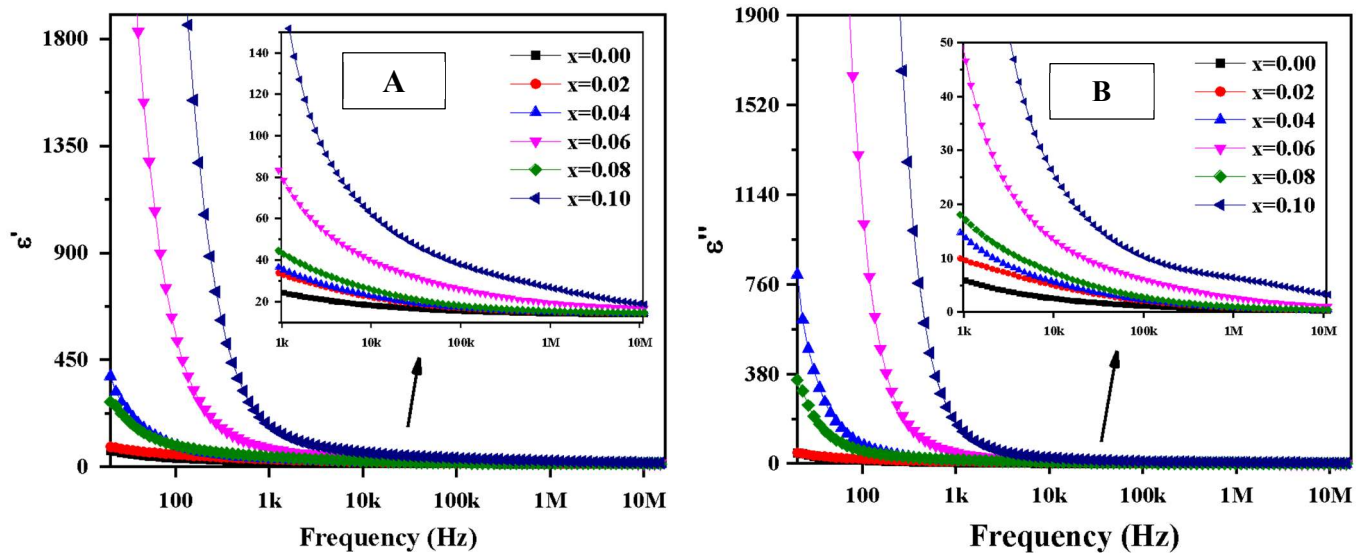


Fig. 6. Extracted initial permeability (A) real and (B) Imaginary part for the investigated nanocrystalline $\text{Ni}_{0.7}\text{Cu}_{0.3}\text{Al}_x\text{Fe}_{2-x}\text{O}_4$.

The sample with $x = 0.1$ shows the maximum value of ϵ' because of the redistribution of Fe^{3+} at both A- and B-sites in $\text{Ni}_{0.70}\text{Cu}_{0.30}\text{Al}_x\text{Fe}_{2-x}\text{O}_4$. The substitution of Fe^{3+} by Al^{3+} in the compositions results the transfer of Al^{3+} at A-sites and replaces some Fe^{3+} at B-sites, which causes the enhancement of Fe^{3+} ions in the grain and assembles them in the grain boundary^{48,61}. Consequently, the space charge polarization is increased and caused a higher value of the dielectric constant. Due to the generation of heat in dielectric materials by the high flow of electricity which is dissipated and considered as the material’s loss that is characterized as the imaginary part (ϵ'') of dielectric constant⁵⁴. From Fig. 6(B), it is observed that the value of ϵ'' increases significantly with increasing Al^{3+} content in ferrites. The decrease of ϵ'' with frequency is occurred due to the

high resistive effect of the grain boundaries. The electrons reverse their direction of motion frequently at higher frequencies and the hopping electrons can no longer follow the applied electric field, the probability of charge transport at the grain boundary decreases, resulting in the decrease of polarization, giving the low value of ϵ'' ^{17,55,60,61}.

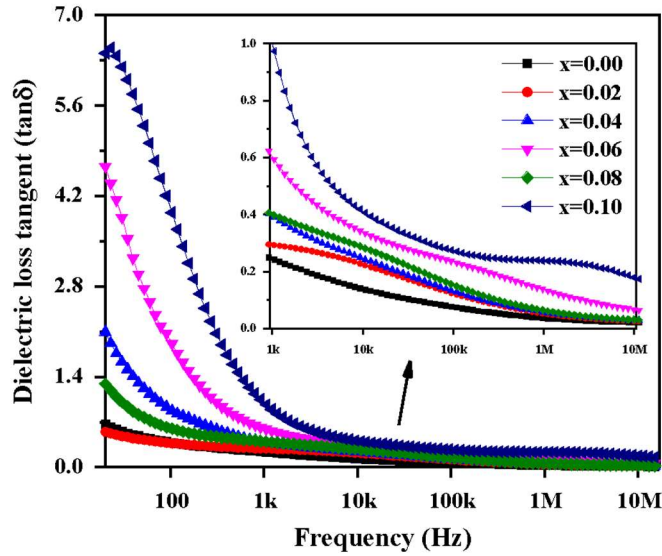


Fig. 7. Dielectric loss tangent vs frequency plot of the synthesized Al^{3+} Ni-Cu NPs.

Fig. 7 shows the variation of dielectric loss tangent ($\tan \delta_E$) of the synthesized samples annealed at 700 °C with varying frequencies. Due to impurities and imperfections, the polarization lags behind the applied voltage, causing $\tan \delta_E$ to form there ^{54,61}. The highest value of $\tan \delta_E$ is found under the relaxation condition of $\omega\tau = 1$, where $\omega = 2\pi f_{max}$, and $\tau = 1/2P$ and f_{max} , τ represents the peak frequency and the relaxation time, respectively and both of which are closely related to the hopping or jumping probability. Electron sharing between Fe^{3+} and Fe^{2+} requires very little energy and the maximum peak is achieved when the hopping frequency between them is well-matched with the applied electric field. Koop's theory explains how $\tan \delta_E$ of the investigated materials decreases with frequency, in a very simple, smooth, and neat way ^{62,63}. It is noted that at lower conductive grain boundaries, $\tan \delta_E$ exhibits the maximum value as more electrons are available to be conductive at the low-frequency region. There is energy loss that occurred during the electrons sharing between Fe^{3+} and Fe^{2+} , therefore high energy is required ^{47,64,65}.

The role of microstructure is important in determining the $\tan\delta_E$. *H. Jia et. al.* showed that the grain boundaries and porosity between polycrystalline crystals affect the ε' and ε'' ⁶⁶. The inter-relation among porosity, grain boundaries, and dielectric loss is defined by the following relation:

$$\tan\delta_E = (1 - P)\tan\delta_o + C_m P^n \quad (22)$$

where C_m is the material-dependent constant, P represents the porosity and $\tan\delta_o$ is the dielectric loss of material with full densification. Uniform density and lower porosity reduce the ε' and ε'' , respectively and the intrinsic and extrinsic fault are responsible for the dielectric loss.

3.4 AC Resistivity

The variation in ac resistivity (ρ_{ac}) of the investigated samples with frequencies (annealed at 700 °C) is depicted in Fig. 8. The variation in ρ_{ac} of the investigated ferrite nanoparticles is explained based on the hopping mechanism. The ρ_{ac} is calculated by the following equation⁵⁴:

$$\rho_{ac} = \frac{1}{\varepsilon_0 \varepsilon' \omega t a_E} \quad (23)$$

where ω defines as the angular frequency. According to the hopping mechanism, electrons jump from one state to another, which prefer to be distributed over the sites in the lattice. In Fig. 8, it is anticipated that at lower frequencies the ρ_{ac} of the investigated ferrites has higher values and depletes with increasing frequency. After a certain frequency, it gets almost saturation with showing a very small value. This variation of ρ_{ac} with frequency can be described by the frequency dependency of grains and grain boundaries. The conductivity mechanism illustrates the particles ability to be highly electrically conductive^{67,68}.

The high-resistive boundary separating the grains are more active at lower frequencies, which impedes the movement of free charges and thus the hopping of electrons between Fe^{2+} and Fe^{3+} is less, which in turns result the higher values of ρ_{ac} ⁵⁴. To increase the hopping of electrons between Fe^{2+} and Fe^{3+} , it must be operated at higher frequencies, which plays a critical role in reducing the ρ_{ac} value. The main reason for the low values of ρ_{ac} is that the hopping of electrons almost stops after a certain frequency range. As depicted in Fig 8, the maximum value of ρ_{ac} is found for the

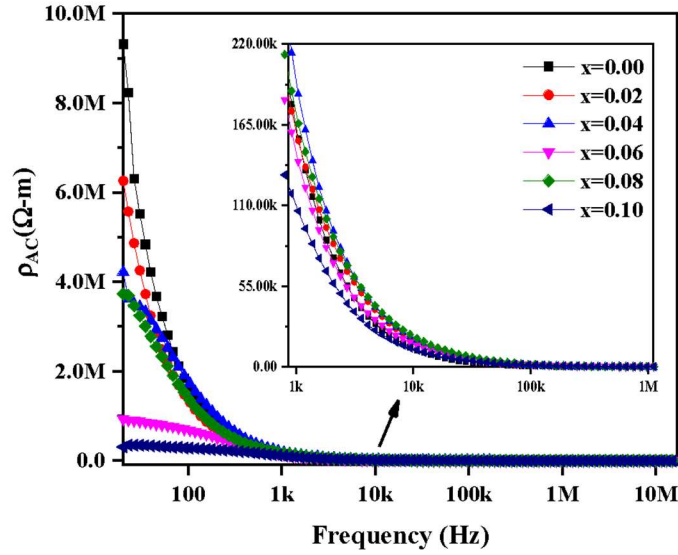


Fig. 8. AC resistivity of the synthesized Al^{3+} substituted Ni-Cu nanoparticles.

mother sample, $Ni_{0.70}Cu_{0.30}Fe_2O_4$. With the increase of Al^{3+} concentration in Ni-Cu ferrites, the AC conductivity increases; therefore $Ni_{0.70}Cu_{0.30}Al_{0.1}Fe_{1.9}O_4$ shows the minimum value at the low-frequency region, and the conduction takes place through highly resistive grain boundaries, while at high frequencies conduction occurs through low resistive grains^{65–67}.

The high-resistive boundary separating the grains are more active at lower frequencies, which impedes the movement of free charges and thus the hopping of electrons between Fe^{2+} and Fe^{3+} is less, which in turns result the higher values of ρ_{ac} ⁵⁴. To increase the hopping of electrons between Fe^{2+} and Fe^{3+} , it must be operated at higher frequencies, which plays a critical role in reducing the ρ_{ac} value. The main reason for the low values of ρ_{ac} is that the hopping of electrons almost stops after a certain frequency range. As depicted in Fig 8, the maximum value of ρ_{ac} is found for the mother sample, $Ni_{0.70}Cu_{0.30}Fe_2O_4$. With the increase of Al^{3+} concentration in Ni-Cu ferrites, the AC conductivity increases; therefore $Ni_{0.70}Cu_{0.30}Al_{0.1}Fe_{1.9}O_4$ shows the minimum value at the low-frequency region, and the conduction takes place through highly resistive grain boundaries, while at high frequencies conduction occurs through low resistive grains^{65–67}.

3.5 Complex Electric Modulus

The electric relaxation mechanism in the materials can be explained through the spectroscopy of electric modulus (M^*), which is resolved into two components⁶³ as given in the following:

$$M^* = \frac{1}{\epsilon^*} = \frac{1}{\epsilon' - i\epsilon''} = \frac{\epsilon'}{\epsilon'^2 + \epsilon''^2} - i \frac{\epsilon''}{\epsilon'^2 + \epsilon''^2} = M' + iM'' \quad (24)$$

where $M' = \frac{\epsilon'}{\epsilon'^2 + \epsilon''^2}$ is the real and $M'' = \frac{\epsilon''}{\epsilon'^2 + \epsilon''^2}$ is the imaginary part of the electric modulus.

From the above equations, both the real (M') and imaginary (M'') parts of modulus are found to be frequency-dependent, which plays a key role in investigating the relaxation mechanism of the materials. From the Fig. 9(A), it is perceived that M' responds very well to higher frequencies with exhibiting the highest value for $x=0.00$. It indicates the lower value of ϵ' at high frequencies. The inadequacy of the restorative force and the release of space charge polarization near the grain boundary helps to attain its saturation. This phenomenon occurs at higher frequencies and at the same time ensures frequency independency in the electrical properties of the materials^{47,63,64}.

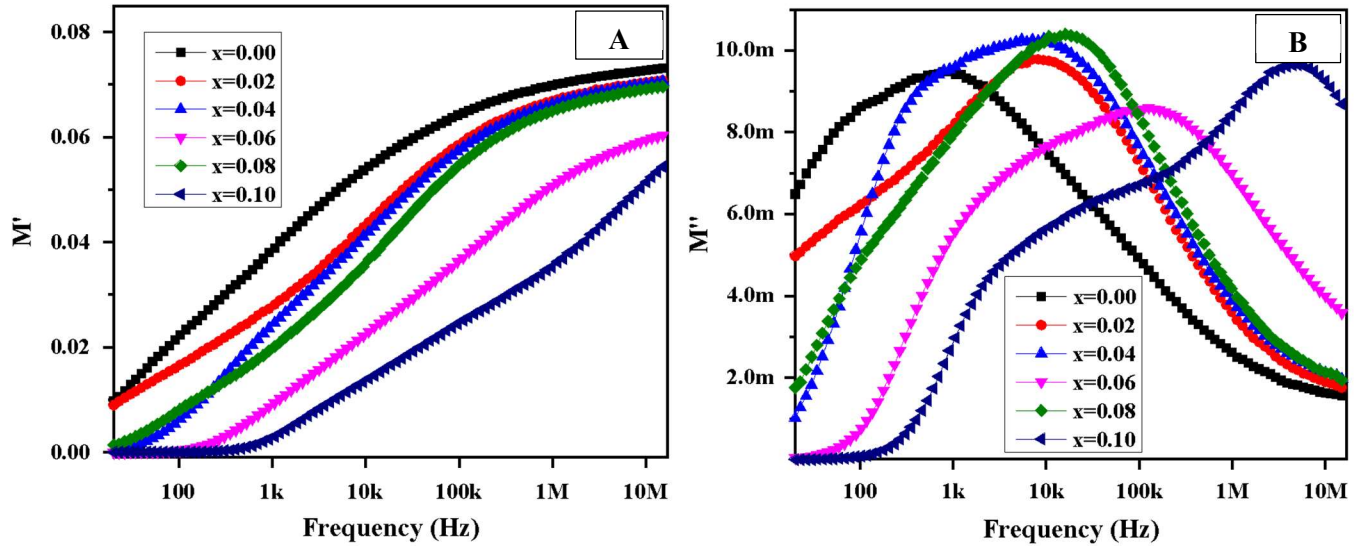


Fig. 9. Electric modulus behavior for the synthesized Al^{3+} substituted Ni-Cu nanoparticles.

To illustrate the peaking behavior, one has to look at the variation of M'' as shown in Fig. 9(B). The hopping mechanism is used to illustrate the peaking behavior better as it more accurately explains the transition of the charge carriers. In the figure above, it is clear and understand that

charge carriers contributing to the hopping process cover long distances at low frequencies. On the other hand, charge carriers are able to cover short distances at higher frequencies, which indicates the relaxation in the polarization process ^{69,70}.

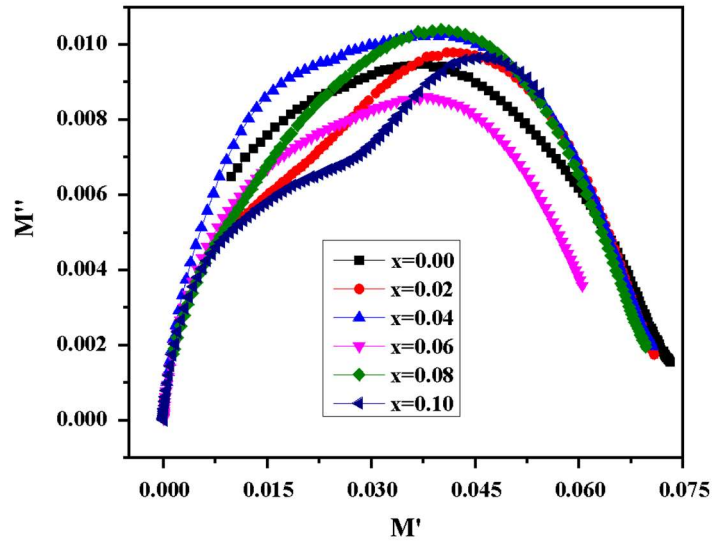


Fig. 10. M'' vs M' plot for the investigated Al^{3+} substituted Ni-Cu NPs.

The relaxation of the material is distinguished by the cole-cole plot (M'' vs M') of the electric modulus as presented in Fig. 10. The grain and grain boundary are thought to be responsible for this separation ^{62,69}. A clear non-Debye type relaxation is found by looking closely at the non-overlapping semicircular pattern in Fig. 10. Nanoparticles annealed at 700 °C show two identical non- overlapping semicircular patterns ⁴⁷.

3.6 Complex Impedance Analysis

To study the electrical behavior of the material, the impedance spectroscopy was employed in this study for the synthesized nanoparticles. This is a long-established method to distinguish the impedance contributions of the materials' grains, grain boundaries and electrodes. The complex impedance (Z^*) includes both the resistive and reactive components of the impedance as follow:

$$Z^*=Z' - jZ'' \quad (25)$$

where the resistive part is designated as the real part Z' which is the horizontal component of the complex impedance denoted as $Z' = |Z^*|\cos\theta$ and the imaginary part is designated as the reactive (capacitive) part expressed as $Z'' = |Z^*|\sin\theta$. However, these two components are combined impedance effect of resistance and capacitance due to grain and grain boundary which are embroiled to dielectric and electric modulus parameters following the relation:

$$\tan\delta = \frac{\varepsilon''}{\varepsilon'} = \frac{Z''}{Z'} = \frac{M''}{M'} \quad (26)$$

The variation in real part of complex impedance (Z') of the investigated ferrites annealed at 700 °C is illustrated in Fig. 11(A) with varying frequencies. The higher values of Z' of synthesized ferrites are revealed at lower frequencies with dispersed behavior and drop sharply up to 1 KHz and thereafter it remains to constant in high frequency.

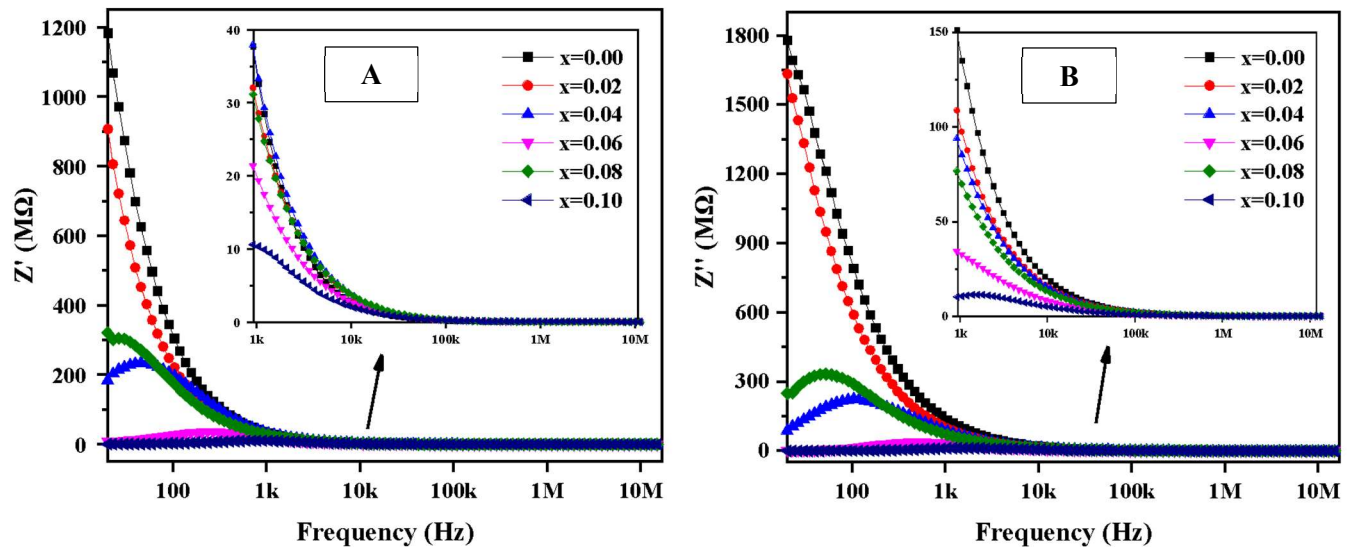


Fig. 11. Impedance analyzer extracted plots for the synthesized Al doped Ni-Cu spinel nano-ferrites.

Besides, in Fig. 11(B), the variation in imaginary part (Z'') of the complex impedance for the synthesized $\text{Ni}_{0.7}\text{Cu}_{0.3}\text{Al}_x\text{Fe}_{2-x}\text{O}_4$ nano-ferrites is illustrated. As observed in Fig 11(B), the materials show higher values at the lower frequency likewise the real part (Z') and decrease rapidly with increasing frequency (up to 10 KHz) as the conductivity of the ferrites increases. However, at higher frequencies ($\geq 100\text{KHz}$), it appears with frequency-independent behavior of small

constant values in effect of the reduction in polarization ^{54,61,71,72}. Both of the Fig. 11 shows the similar trend to the dielectric nature of the materials. For all compositions, the impedance curves are appeared to merge at higher frequencies indicating the predominance contribution of low resistive grains. Moreover, the space-charge polarization is considered important only when the materials are resolved into grains and grain boundaries ^{61,68}. The curves tend to converge at higher frequencies owing to a decrease in space charge polarization and this behavior elucidates the increasing tendency of ac conductivity with frequency, confirming the semiconducting behavior of the prepared nanocrystalline spinel ferrites ^{47,71}.

The Nyquist impedance plot (also known as cole-cole plot) of the prepared $\text{Ni}_{0.7}\text{Cu}_{0.3}\text{Al}_x\text{Fe}_{2-x}\text{O}_4$ ferrites annealed at 700 °C is shown in Fig. 12 which reveals the contribution of grain and grain boundary resistance as the plot is combined response of RC circuit by parallely connected resistor and capacitor. The heterostructure nature of synthesized materials along with characteristic nature of complex impedance spectra by determining the existence of multiple electrical responses (due to grain resistance R_g , grain boundary resistance R_{gb} and electrode effects) can be easily determined by observing the semicircular arcs appeared in the cole-cole plot ^{47,54,72}. By looking at Fig. 12, the two semicircular arcs are clearly visible which are formed with its center placed below the real axis, which manifests the single-phase of Al^{3+} substituted nanocrystalline Ni-Cu materials. The diameter of the semicircle arcs is found to decrease with increasing Al^{3+} concentration, which is actually caused by the resistance of grain boundaries. However, at lower frequencies, the R_g dominates the appearance of the first semicircle, whereas at higher frequencies, the R_{gb} dominates the appearance of the second semicircle. The difference in relaxation time is considered as the main catalyst behind the separation of semicircles arcs ⁶¹.

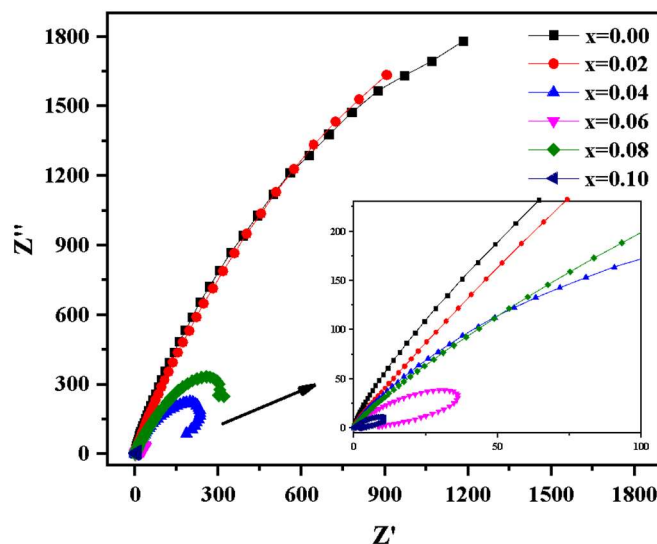


Fig. 12. Nyquist impedance plot of the prepared Ni-Cu ferrites annealed at 700 °C

Conclusion

The sol gel method was used to synthesize a series of high crystalline nanomaterials of $\text{Ni}_{0.7}\text{Cu}_{0.30}\text{Al}_x\text{Fe}_{2-x}\text{O}_4$. The single-phase cubic spinel structure of the investigated materials was confirmed through XRD study with no impurity. The surface morphology was studied through the FESEM measurements, which illustrated the distribution of semi-spherical grains separated by the grain boundaries with a homogenous distribution of particles on the surface. The structural parameters were determined using the XRD and FESEM data. The electrical and dielectric properties were carried out by using the impedance analyzer supported with the modulus and impedance spectroscopy. Both the average crystallite size and the average grain size of the studied materials are found in the nano-scale range (55.63–70.74 nm) and (59.00– 65.00 nm), respectively. The dielectric dispersion nature of the materials was revealed through the dielectric study of the materials. The electrical response of the materials was inspected by means of impedance and modulus spectroscopy, which well resolved the contribution of grains and grain boundaries in the electrical properties of the investigated Al^{3+} substituted Ni-Cu ferrite nanoparticles. The relaxation phenomena in the materials was justified through the cole-cole analysis of both impedance and

modulus spectra. A little substitution of Al^{3+} is found to be influential in the structural, dielectric and electrical properties of Ni-Cu spinel ferrites prepared by the cost-effective sol gel method.

Acknowledgment

The authors are grateful to the center of excellence of the Department of Mathematics and Physics at North South University (NSU), Dhaka 1229, Bangladesh. This research is funded by the NSU research grant CTRG-20/SEPS/13.

Data Availability

The authors are currently using all related data for the purpose of further research. If the data is requested, the authors are ready to share it with the publisher.

Reference:

1. Elshahawy, A. M., Mahmoud, M. H., Makhlof, S. A. & Hamdeh, H. H. Role of Cu^{2+} substitution on the structural and magnetic properties of Ni-ferrite nanoparticles synthesized by the microwave-combustion method. *Ceramics International* **41**, 11264–11271 (2015).
2. Atiq, S. *et al.* Synthesis and investigation of structural, morphological, magnetic, dielectric and impedance spectroscopic characteristics of Ni-Zn ferrite nanoparticles. *Ceramics International* **43**, 2486–2494 (2017).
3. Ditta, A., Khan, M. A., Junaid, M., Khalil, R. M. A. & Warsi, M. F. Structural, magnetic and spectral properties of Gd and Dy co-doped dielectrically modified Co-Ni ($\text{Ni}_{0.4}\text{Co}_{0.6}\text{Fe}_2\text{O}_4$) ferrites. *Physica B: Condensed Matter* **507**, 27–34 (2017).
4. Jalaiah, K. & Vijaya Babu, K. Structural, magnetic and electrical properties of nickel doped Mn-Zn spinel ferrite synthesized by sol-gel method. *Journal of Magnetism and Magnetic Materials* **423**, 275–280 (2017).
5. Rodrigues, A. P. G. *et al.* Nanoferrites of nickel doped with cobalt: Influence of Co^{2+} on the structural and magnetic properties. *Journal of Magnetism and Magnetic Materials* **374**, 748–754 (2015).
6. Pardavi-Horvath, M. Microwave applications of soft ferrites. *Journal of Magnetism and Magnetic Materials* **215–216**, 171–183 (2000).
7. Narang, S. B. & Pubby, K. Nickel Spinel Ferrites: A review. *Journal of Magnetism and Magnetic Materials* **519**, 167163 (2021).
8. Silva, F. G. da *et al.* Structural and Magnetic Properties of Spinel Ferrite Nanoparticles. *Journal of Nanoscience and Nanotechnology* **19**, 4888–4902 (2019).

9. Qindeel, R., Alonizan, N. H., Alghamdi, E. A. & Awad, M. A. Synthesis and characterization of spinel ferrites for microwave devices. *Journal of Sol-Gel Science and Technology* **97**, 593–599 (2021).
10. Tang, C. *et al.* Application of magnetic nanoparticles in nucleic acid detection. *Journal of Nanobiotechnology* **18**, 62 (2020).
11. Hashim, Mohd. *et al.* Investigation of structural, dielectric, magnetic and antibacterial activity of Cu–Cd–Ni–FeO₄ nanoparticles. *Journal of Magnetism and Magnetic Materials* **341**, 148–157 (2013).
12. Majidi, S. *et al.* Magnetic nanoparticles: Applications in gene delivery and gene therapy. *Artificial Cells, Nanomedicine, and Biotechnology* 1–8 (2015)
doi:10.3109/21691401.2015.1014093.
13. Batoo, K. M. & Ansari, M. S. Low temperature-fired Ni-Cu-Zn ferrite nanoparticles through auto-combustion method for multilayer chip inductor applications. *Nanoscale Research Letters* **7**, 112 (2012).
14. Šepelák, V., Heitjans, P. & Becker, K. D. Nanoscale spinel ferrites prepared by mechanochemical route. *Journal of Thermal Analysis and Calorimetry* **90**, 93–97 (2007).
15. Baskar, S., Yuvaraj, S., Sundararajan, M. & Sekhar Dash, C. Influence of Ca²⁺ Ion Substitution on Structural, Morphological, Optical, Thermal and Magnetic Behaviour of Mg_{1-x}Ca_xFe₂O₄ (0 ≤ x ≤ 0.5) Spinel. *Journal of Superconductivity and Novel Magnetism* **33**, 3949–3956 (2020).
16. Lal, G. *et al.* Structural, cation distribution, optical and magnetic properties of quaternary Co_{0.4+x}Zn_{0.6-x}Fe₂O₄ (x = 0.0, 0.1 and 0.2) and Li doped quinary Co_{0.4+x}Zn_{0.5-x}Li_{0.1}Fe₂O₄ (x = 0.0, 0.05 and 0.1) nanoferrites. *Journal of Alloys and Compounds* **828**, 154388 (2020).
17. Arifuzzaman, M., Hossen, M. B., Harun-Or-Rashid, Md. & Rahman, M. L. Structural and magnetic properties of nanocrystalline Ni_{0.7-x}Cu_xCd_{0.3}Fe₂O₄ prepared through Sol-gel method. *Materials Characterization* **171**, 110810 (2021).
18. Sanpo, N., Wen, C., Berndt, C. C. & Wang, J. Multifunctional Spinel Ferrite Nanoparticles for Biomedical Application. in *Advanced Functional Materials* 183–217 (John Wiley & Sons, Inc., 2015). doi:10.1002/9781118998977.ch4.
19. Sharma, H. R. *et al.* Structural, electrical, and magnetic studies of Cu²⁺ substituted MnFe₂O₄ nanoferrites synthesized via solution combustion technique. *Journal of Materials Science: Materials in Electronics* **33**, 7528–7542 (2022).
20. Batoo, K. M. *et al.* Hyperfine interaction and tuning of magnetic anisotropy of Cu doped CoFe₂O₄ ferrite nanoparticles. *Journal of Magnetism and Magnetic Materials* **411**, 91–97 (2016).
21. Farea, A. M. M. *et al.* Structure and electrical properties of Co_{0.5}Cd_xFe_{2.5-x}O₄ ferrites. *Journal of Alloys and Compounds* **464**, 361–369 (2008).
22. Asiri, S. *et al.* Hydrothermal synthesis of Co_yZn_yMn_{1-2y}Fe₂O₄ nanoferrites: Magneto-optical investigation. *Ceramics International* **44**, 5751–5759 (2018).

23. Battoo, K. M. & El-sadek, M.-S. A. Electrical and magnetic transport properties of Ni–Cu–Mg ferrite nanoparticles prepared by sol–gel method. *Journal of Alloys and Compounds* **566**, 112–119 (2013).
24. Sarveena *et al.* Room temperature long range ferromagnetic ordering in Ni_{0.58}Zn_{0.42}Co_{0.10}Cu_{0.10}Fe_{1.8}O₄ nano magnetic system. in 050114 (2015). doi:10.1063/1.4917755.
25. Yonatan Mulushoa, S. *et al.* Structural, dielectric and magnetic properties of Nickel-Chromium substituted Magnesium ferrites, Mg₁–Ni Fe₂-xCr_xO₄ (0 ≤ x ≤ 0.7). *Inorganic Chemistry Communications* **138**, 109289 (2022).
26. Ch., R. *et al.* Effect of La-Cu co-substitution on structural, microstructural and magnetic properties of M-type strontium hexaferrite (Sr₁–xLa_xFe₁₂–xCu_xO₁₉). *Inorganic Chemistry Communications* **134**, 109053 (2021).
27. Boda, N. *et al.* Effect of rare earth elements on low temperature magnetic properties of Ni and Co-ferrite nanoparticles. *Journal of Magnetism and Magnetic Materials* **473**, 228–235 (2019).
28. Yonatan Mulushoa, S. *et al.* Structural, dielectric and magnetic properties of Nickel-Chromium substituted Magnesium ferrites, Mg₁–xNi_xFe₂-xCr_xO₄ (0 ≤ x ≤ 0.7). *Inorganic Chemistry Communications* **138**, 109289 (2022).
29. Munir, S. *et al.* Synthesis, characterization and photocatalytic parameters investigation of a new CuFe₂O₄/Bi₂O₃ nanocomposite. *Ceramics International* **46**, 29182–29190 (2020).
30. Lee, J. E., Han, S. I. & Hyeon, T. Magnetically recyclable hollow nanocomposite catalysts for heterogeneous reduction of nitroarenes and Suzuki reactions. *Chemical Communications* **49**, 4779–4781 (2013).
31. Rahman, A., Warsi, M. F., Shakir, I., Shahid, M. & Zulfiqar, S. Fabrication of Ce³⁺ substituted nickel ferrite-reduced graphene oxide heterojunction with high photocatalytic activity under visible light irradiation. *Journal of Hazardous Materials* **394**, 122593 (2020).
32. Bharati, V. A. *et al.* Influence of trivalent Al–Cr co-substitution on the structural, morphological and Mössbauer properties of nickel ferrite nanoparticles. *Journal of Alloys and Compounds* **821**, 153501 (2020).
33. Bashir, K. B. *et al.* Effect of Cr³⁺ substitution on magnetic and electrical properties of (Ni_{0.3}Cu_{0.7}) Fe₂O₄ spinel ferrites. *Revista Mexicana de Física* **66**, 573–579 (2020).
34. Li, L.-Z., Zhong, X.-X., Wang, R., Tu, X.-Q. & He, L. Effects of Al substitution on the properties of NiZnCo ferrite nanopowders. *Journal of Materials Science: Materials in Electronics* **29**, 7233–7238 (2018).
35. Vigneswari, T. & Raji, P. Structural, magnetic and optical properties of Al-substituted nickel ferrite nanoparticles. *International Journal of Materials Research* **109**, 413–421 (2018).

36. Islam, M. R. *et al.* Effect of Al doping on the structural and optical properties of CuO nanoparticles prepared by solution combustion method: Experiment and DFT investigation. *Journal of Physics and Chemistry of Solids* **147**, 109646 (2020).
37. Gul, S. *et al.* Al-substituted zinc spinel ferrite nanoparticles: Preparation and evaluation of structural, electrical, magnetic and photocatalytic properties. *Ceramics International* **46**, 14195–14205 (2020).
38. Rather, S. ullah & Lemine, O. M. Effect of Al doping in zinc ferrite nanoparticles and their structural and magnetic properties. *Journal of Alloys and Compounds* **812**, 152058 (2020).
39. Han, T.-C., Tu, Z.-Y. & Huang, Y.-T. Enhanced magnetic and magnetodielectric properties of Al-doped gallium ferrite nanoparticles. *AIP Advances* **10**, 015213 (2020).
40. Kumar, L. & Kar, M. Influence of Al³⁺ ion concentration on the crystal structure and magnetic anisotropy of nanocrystalline spinel cobalt ferrite. *Journal of Magnetism and Magnetic Materials* **323**, 2042–2048 (2011).
41. Kuanr, B. K. *et al.* Frequency and field dependent dynamic properties of CoFe_{2-x}Al_xO₄ ferrite nanoparticles. *Materials Research Bulletin* **76**, 22–27 (2016).
42. Zare, S., Ati, A. A., Dabagh, S., Rosnan, R. M. & Othaman, Z. Synthesis, structural and magnetic behavior studies of Zn–Al substituted cobalt ferrite nanoparticles. *Journal of Molecular Structure* **1089**, 25–31 (2015).
43. Kumari, N., Kumar, V. & Singh, S. K. Dielectric study of Al³⁺ substituted Fe₃O₄ ferrite nanoparticles. *International Journal of Modern Physics B* **28**, 1450193 (2014).
44. Ateia, Ebtesam. E. & Mohamed, Amira. T. Nonstoichiometry and phase stability of Al and Cr substituted Mg ferrite nanoparticles synthesized by citrate method. *Journal of Magnetism and Magnetic Materials* **426**, 217–224 (2017).
45. Hashim, Mohd. *et al.* Structural, magnetic and electrical properties of Al³⁺ substituted Ni–Zn ferrite nanoparticles. *Journal of Alloys and Compounds* **511**, 107–114 (2012).
46. Birajdar, A. A. *et al.* Permeability and magnetic properties of Al³⁺ substituted Ni_{0.7}Zn_{0.3}Fe₂O₄ nanoparticles. *Journal of Applied Physics* **112**, 053908 (2012).
47. Ahmed, S. K., Mahmood, M. F., Arifuzzaman, M. & Belal Hossen, M. Enhancement of electrical and magnetic properties of Al³⁺ substituted CuZn nano ferrites with structural Rietveld refinement. *Results in Physics* **30**, 104833 (2021).
48. Rahman, K. R., Chowdhury, F.-U.-Z. & Khan, M. N. I. Influence of Al³⁺ substitution on the electrical resistivity and dielectric behavior of Ni_{0.25}Cu_{0.20}Zn_{0.55}Al_xFe_{2-x}O₄ ferrites synthesized by solid state reaction technique. *Journal of Magnetism and Magnetic Materials* **443**, 366–373 (2017).
49. Ashraf, N. *et al.* Wafer-Like CoS Architectures and Their Nanocomposites with Polypyrrole for Electrochemical Energy Storage Applications. *ChemistrySelect* **5**, 8129–8136 (2020).

50. Aadil, M. *et al.* Enhanced electrochemical energy storage properties of carbon coated Co₃O₄ nanoparticles-reduced graphene oxide ternary nano-hybrids. *Ceramics International* **46**, 17836–17845 (2020).
51. Hoque, S. M., Choudhury, Md. A. & Islam, Md. F. Characterization of Ni–Cu mixed spinel ferrite. *Journal of Magnetism and Magnetic Materials* **251**, 292–303 (2002).
52. Krishnamoorthy, K., Veerasubramani, G. K. & Kim, S. J. Hydrothermal synthesis, characterization and electrochemical properties of cobalt sulfide nanoparticles. *Materials Science in Semiconductor Processing* **40**, 781–786 (2015).
53. Kumar, L., Kumar, P., Narayan, A. & Kar, M. Rietveld analysis of XRD patterns of different sizes of nanocrystalline cobalt ferrite. *International Nano Letters* **3**, 8 (2013).
54. Harun-Or-Rashid, Md., Rahman, Md. M., Arifuzzaman, M. & Hossain, A. K. M. A. Structural, magnetic, and electrical properties of Ni_{0.38–x}Cu_{0.15+y}Zn_{0.47+x–y}Fe₂O₄ synthesized by sol–gel auto-combustion technique. *Journal of Materials Science: Materials in Electronics* (2021) doi:10.1007/s10854-021-05953-z.
55. Anwar, A. *et al.* The impact of highly paramagnetic Gd³⁺ cations on structural, spectral, magnetic and dielectric properties of spinel nickel ferrite nanoparticles. *Journal of Saudi Chemical Society* **25**, 101306 (2021).
56. Naik, M. M. *et al.* Effect of aluminium doping on structural, optical, photocatalytic and antibacterial activity on nickel ferrite nanoparticles by sol–gel auto-combustion method. *Journal of Materials Science: Materials in Electronics* **29**, 20395–20414 (2018).
57. Muniba *et al.* Aluminum Substitution in Ni-Co Based Spinel Ferrite Nanoparticles by Sol–Gel Auto-Combustion Method. *Journal of Electronic Materials* **50**, 3302–3311 (2021).
58. Sathiya Priya, A., Geetha, D. & Kavitha, N. Effect of Al substitution on the structural, electric and impedance behavior of cobalt ferrite. *Vacuum* **160**, 453–460 (2019).
59. Gabal, M. A., al Angari, Y. M., Obaid, A. Y. & Qusti, A. Structural analysis and magnetic properties of nanocrystalline NiCuZn ferrites synthesized via a novel gelatin method. *Advanced Powder Technology* **25**, 457–461 (2014).
60. Ali, M. A., Uddin, M. M., Khan, M. N. I., Chowdhury, F.-U.-Z. & Haque, S. M. Structural, morphological and electrical properties of Sn-substituted Ni-Zn ferrites synthesized by double sintering technique. *Journal of Magnetism and Magnetic Materials* **424**, 148–154 (2017).
61. Harun-Or-Rashid, Md., Islam, M. N., Arifuzzaman, M. & Hossain, A. K. M. A. Effect of sintering temperature on the structural, morphological, electrical, and magnetic properties of Ni–Cu–Zn and Ni–Cu–Zn–Sc ferrites. *Journal of Materials Science: Materials in Electronics* **32**, 2505–2523 (2021).
62. Rayssi, Ch., El.Kossi, S., Dhahri, J. & Khirouni, K. Frequency and temperature-dependence of dielectric permittivity and electric modulus studies of the solid solution Ca_{0.85}Er_{0.1}Ti_{1–x}Co_{4x/3}O₃ (0 ≤ x ≤ 0.1). *RSC Advances* **8**, 17139–17150 (2018).

63. Kaiser, M. Electrical conductivity and complex electric modulus of titanium doped nickel–zinc ferrites. *Physica B: Condensed Matter* **407**, 606–613 (2012).
64. Nitika & Rana, A. Study of anneal-tuned dielectric properties, AC conductivity, complex impedance, and modulus of cobalt ferrite nanoparticles. *Materials Today: Proceedings* **45**, 5444–5448 (2021).
65. Butt, K. Y. *et al.* The study of structural, magnetic and dielectric properties of spinel ferrites for microwave absorption applications. *Applied Physics A* **127**, 714 (2021).
66. Jia, H. *et al.* Monodomain MgCuZn ferrite with equivalent permeability and permittivity for broad frequency band applications. *Ceramics International* **43**, 5974–5978 (2017).
67. Santhosh Kumar, M. V. *et al.* Induced effects of Zn²⁺ on the transport and complex impedance properties of Gadolinium substituted nickel-zinc nano ferrites. *Journal of Magnetism and Magnetic Materials* **478**, 12–19 (2019).
68. Rashid, M. H. & Hossain, A. K. M. A. Structural, morphological and electromagnetic properties of Sc³⁺ doped Ni-Cu-Zn ferrites. *Results in Physics* **11**, 888–895 (2018).
69. Oumezzine, E., Hcini, S., Rhouma, F. I. H. & Oumezzine, M. Frequency and temperature dependence of conductance, impedance and electrical modulus studies of Ni_{0.6}Cu_{0.4}Fe₂O₄ spinel ferrite. *Journal of Alloys and Compounds* **726**, 187–194 (2017).
70. Dutta, A. & Sinha, T. P. Dielectric relaxation in perovskite. *Journal of Physics and Chemistry of Solids* **67**, 1484–1491 (2006).
71. Channa, N. *et al.* Structural, dielectric, impedance, and electric modulus properties of Cu²⁺-substituted Cu_xMn_{1-x}Fe₂O₄ spinel ferrites nanoparticles. *Journal of Materials Science: Materials in Electronics* **32**, 2832–2844 (2021).
72. Dabbebi, T. *et al.* Investigations of microstructural and impedance spectroscopic properties of Mg_{0.5}Co_{0.5}Fe_{1.6}Al_{0.4}O₄ ferrite prepared using sol–gel method. *Journal of Materials Science: Materials in Electronics* **32**, 12521–12534 (2021).